EUROPEAN ORGANISATION FOR NUCLEAR RESEARCH (CERN)

Submitted to: Phys. Lett. B.

CERN-EP-2022-208
10th March 2023

Probing the CP nature of the top–Higgs Yukawa coupling in $t\bar{t}H$ and tH events with $H \to b\bar{b}$ decays using the ATLAS detector at the LHC

The ATLAS Collaboration

The CP properties of the coupling between the Higgs boson and the top quark are investigated with 139 fb^{-1} of proton–proton collision data recorded by the ATLAS experiment at the LHC at a centre-of-mass energy of $\sqrt{s}$ = 13 TeV. The CP structure of the top quark–Higgs boson Yukawa coupling is probed in events with a Higgs boson decaying into a pair of b-quarks and produced in association with either a pair of top quarks, $t\bar{t}H$, or a single top quark, tH. Events containing one or two electrons or muons are used for the measurement. In an extension of the Standard Model with a CP-odd admixture to the top–Higgs Yukawa coupling, the mixing angle between CP-even and CP-odd couplings is measured to be $\alpha = 11\,^{\circ+52^{\circ}}_{-73^{\circ}}$.

1 Introduction

Since the observation of the Higgs boson at the LHC [1, 2], its properties have been studied in great detail. In particular, the observation of the Higgs boson production in association with a top-quark pair, $t\bar{t}H$ [3, 4], provides direct experimental access to the top-quark Yukawa coupling at the tree-level. The increasing datasets at the LHC have recently allowed the ATLAS and CMS Collaborations to probe the charge-conjugation and parity (CP) properties of this coupling using $t\bar{t}H$ events with $H \to \gamma\gamma$ decays [5, 6]. This letter reports on a study of the CP properties of the top-quark Yukawa coupling using $t\bar{t}H$ and tH production, in the $H \to b\bar{b}$ decay channel. The analysis targets final states where at least one top quark decays semi-leptonically to electrons or muons. It uses $\sqrt{s} = 13$ TeV pp collision data recorded by the ATLAS experiment during Run 2, corresponding to an integrated luminosity of 139 fb^{-1}.

The Standard Model (SM) predicts the Higgs boson to be a scalar particle with quantum numbers $J^{CP} = 0^{++}$. Considering the possibility of beyond the Standard Model (BSM) couplings, a CP-odd component of the vector-boson couplings to the Higgs boson is naturally suppressed by the scale at which new physics would become relevant. This suppression does not happen for Yukawa couplings, where CP-odd Higgs–fermion couplings may be significant already at tree level [7]. Experimentally, pure CP-odd couplings of the Higgs boson to vector bosons have been ruled out [8–14]. Analyses of $t\bar{t}H$ events with $H \to \gamma\gamma$ decays [5, 6] have also excluded pure CP-odd top–Higgs couplings at more than a 3 σ significance. But mixing of CP-odd and CP-even states has not been ruled out and is worth investigating. The observation of a non-zero CP-odd coupling component would in fact signal the existence of physics beyond the SM, and open up the possibility of CP-violation in the Higgs sector [15–18]. Such a new source of CP violation could play a fundamental role in explaining the matter–antimatter asymmetry of the universe. Events targeted in this analysis are sensitive to the top–Higgs coupling at the tree-level. This avoids the need for assumptions about the influence of BSM effects which may be present in other, more indirect measurements [19–21]. In particular, current limits on electron and neutron electrical dipole moments place indirect model-dependent constraints on a possible pseudoscalar component of the top-quark Yukawa coupling [22–24].

The top–Higgs interaction can be extended beyond the SM as [19]:

$$\mathcal{L}_{t\bar{t}H} = -\kappa_t' y_t \phi \bar{\psi}_t (\cos\alpha + i\gamma_5 \sin\alpha)\psi_t \,, \tag{1}$$

where y_t is the SM Yukawa coupling strength, modified by a coupling modifier κ_t'; α is the CP-mixing angle; ϕ is the Higgs field; ψ_t and $\bar{\psi}_t$ are top-quark spinor fields and γ_5 is a Dirac matrix. The above expression reduces to the SM case for $\kappa_t' = 1$ and $\alpha = 0$. An anomalous value of α would produce an admixture with a pseudoscalar coupling ($J^{CP} = 0^{+-}$) and change the differential cross-section relative to the SM expectation, while a variation of κ_t' would induce a change in the total cross-section [15, 25–28].

This study measures the values of κ_t' and α with a binned profile likelihood fit. It closely follows a recent analysis optimised for the measurement of the $t\bar{t}H(\to b\bar{b})$ production cross-section [29]. This analysis studies an identical phase space using the same physics object definitions and a similar methodology for event selection and evaluation of systematic uncertainties with respect to that cross-section measurement. A notable exception is that this analysis considers both the $t\bar{t}H$ and tH production modes as signals. No attempt was made to optimise the analysis strategy for the tH signal, as its small yield makes this channel relevant only in one analysis region (see below). Other noteworthy differences with respect to the analysis documented in Ref. [29] are detailed in the text. These include the definition of signal regions, the signal-background discrimination strategy and a few details in the definition of systematic uncertainties in signal and background modelling. In the case of tH production, the destructive interference between the

diagrams with t–H and W–H couplings leads to the negligible tH production cross-section in the SM. Any change in the relative t–H and W–H coupling strengths would result in a rapid increase in the cross-section. Considering the Lagrangian density in Eqn. 1, the tH production cross-section is expected to grow for values of the mixing angle α different from zero [16]. An opposite and less pronounced dependence exists for the $t\bar{t}H$ cross-section. The ratio of tH to $t\bar{t}H$ cross-sections varies from 0.06 in the SM scenario to more than 1.2 in the pure CP-odd scenario [16]. For the present measurement, the $H \to b\bar{b}$ branching ratio is assumed to be equal to its SM value of 58.2% ± 0.5% [30].

2 The ATLAS experiment

The ATLAS experiment [31–33] at the LHC is a multipurpose particle detector with a forward–backward symmetric cylindrical geometry and a near 4π coverage in solid angle.[1] It consists of an inner tracking detector surrounded by a thin superconducting solenoid providing a 2 T axial magnetic field, electromagnetic and hadron calorimeters and a muon spectrometer. A two-level trigger system is used to reduce the total event rate to 1 kHz on average, depending on the data-taking conditions [34]. An extensive software suite [35] is used in the reconstruction and analysis of real and simulated data, in detector operations, and in the trigger and data acquisition systems of the experiment. The events used in this analysis are selected using single-lepton triggers [36, 37], with either low thresholds for the lepton transverse momentum (p_{T}) and a lepton isolation requirement, or higher thresholds, looser identification criteria and without any isolation requirement. The lowest p_{T} threshold for muons is 20 (26) GeV, while for electrons the threshold is 24 (26) GeV for the data taken in 2015 (2016–2018).

3 Event preselection

Events are required to have at least one primary vertex, formed by two or more associated tracks with transverse momenta greater than 0.5 GeV. The vertex with the highest sum of p_{T}^2 of associated tracks is selected as the hard-scattering primary vertex. Events with exactly one lepton (electrons or muons, denoted as ℓ) or two oppositely charged leptons are considered in this analysis, referred to as the ℓ+jets channel and dilepton channel, respectively. Electrons are identified using the 'Tight' likelihood criterion [38] and are required to have $p_{\mathrm{T}} > 10$ GeV and $|\eta| < 2.47$, excluding those in the calorimeter barrel–endcap transition region ($1.37 < |\eta| < 1.52$). Muons are selected with the 'Medium' identification criterion [39] and are required to have $p_{\mathrm{T}} > 10$ GeV and $|\eta| < 2.5$. Electrons (muons) are required to pass the 'Gradient' ('Fixed-Cut-Tight-Track-Only') isolation requirements [38, 39]. All leptons are required to originate from the primary vertex. At least one of the leptons must have $p_{\mathrm{T}} > 27$ GeV and match the corresponding lepton used in the trigger decision. In events with an ee or $\mu\mu$ pair, the dilepton invariant mass is required to be above 15 GeV and outside the Z boson mass window of 83–99 GeV.

This analysis targets events with high jet multiplicities, including b-quark jets expected in the final state of $t\bar{t}H$ and tH events with a subsequent $H \to b\bar{b}$ decay. Following the same procedure as Ref. [29],

[1] ATLAS uses a right-handed coordinate system with its origin at the nominal interaction point (IP) in the centre of the detector and the z-axis along the beam pipe. The x-axis points from the IP to the centre of the LHC ring, and the y-axis points upwards. Cylindrical coordinates (r, ϕ) are used in the transverse plane, ϕ being the azimuthal angle around the z-axis. The momentum component in the transverse plane is referred to as the transverse momentum (p_{T}). The pseudorapidity is defined in terms of the polar angle θ as $\eta = -\ln\tan(\theta/2)$. Angular distance is measured in units of $\Delta R \equiv \sqrt{(\Delta\eta)^2 + (\Delta\phi)^2}$.

jets are reconstructed from topological clusters of energy depositions in the calorimeter [40, 41] using the anti-k_t algorithm [42, 43] with a radius parameter of $R = 0.4$. The MV2c10 algorithm [44] was used to identify (or 'b-tag') jets containing b-hadrons. By placing different selections on the MV2c10 discriminant, four selections are defined with average b-jet tagging efficiencies of 60%, 70%, 77% and 85% and different c- and light-jet rejection rates. The corresponding efficiencies and rejection rates are calibrated to data [44–46]. In the ℓ+jets (dilepton) channel, events are required to have at least five (three) jets with $p_{\mathrm{T}} > 25$ GeV and $|\eta| < 2.5$, and at least four (three) of the jets are required to be b-tagged at the 70% efficiency working point.

The missing transverse momentum is reconstructed as the negative vector sum of the p_{T} of all selected objects in the event, with an extra 'soft term' built from additional tracks associated with the primary vertex [47].

The analysis also exploits the collimated decay topology from high-p_{T} Higgs bosons. Jets with a radius parameter of $R = 0.4$ are reclustered [48] using the anti-k_t algorithm with a radius parameter of $R = 1.0$. The resulting jets are referred to as *large-R* jets. The large-R jets are required to have a mass larger than 50 GeV, $p_{\mathrm{T}} > 200$ GeV and at least two constituent jets with $R = 0.4$.

4 Signal and background modelling

After applying the above selection criteria, background events are dominated by $t\bar{t}$ production with additional jets ($t\bar{t}$+jets), that contain heavy-flavour hadrons (b- and c-hadrons). Other processes contribute less than 10% of the total expected background. All background processes are estimated using Monte Carlo (MC) simulations, closely following Ref. [29].

The simulated events were produced using the ATLAS detector simulation [49] based on Geant4 [50]. To simulate the effects of multiple interactions in the same and neighbouring bunch crossings (pile-up), additional interactions were generated using Pythia 8.186 [51] with a set of tuned parameters called the A3 tune [52] and overlaid on the simulated hard-scatter event. Simulated events are reweighted to match the pile-up conditions observed in the full Run 2 dataset. All simulated event samples are processed through the same reconstruction algorithms and analysis chain as the data [35].

Events in the simulated $t\bar{t}$+jets background sample are categorised according to the flavour of the additional jets which do not originate from the top-quark decay. The simulation of each set of backgrounds is treated independently as this allows for a more accurate modelling of $t\bar{t}$+jets events. The categorisation is based on 'MC-truth jets' that are clustered with stable generated particles (with mean lifetime $\tau > 3 \times 10^{-11}$ s) in the final state using the anti-k_t algorithm with $R = 0.4$. MC-truth jets with $p_{\mathrm{T}} > 15$ GeV and $|\eta| < 2.5$ in the simulated events are used for the categorisation. Their MC-truth flavour is determined by counting the number of b/c-hadrons contained within $\Delta R = 0.4$ of the jet axis. Events with at least one MC-truth jet containing b-hadrons not originating from a top-quark decay are labelled as $t\bar{t} + \geq 1b$. This can be further separated into subcomponents corresponding to $t\bar{t} + 1b$ and $t\bar{t} + \geq 2b$. Events failing to satisfy that criterion but with at least one MC-truth jet containing c-hadrons not originating from top-quark decay are labelled $t\bar{t} + \geq 1c$. The rest of the events are labelled as $t\bar{t}$+light. The dominant $t\bar{t} + \geq 1b$ background is modelled using a sample of $t\bar{t} + b\bar{b}$ events generated at next-to-leading order (NLO) in QCD in the four-flavour scheme, with two additional massive b-quarks produced at the matrix element (ME) level. The ME simulation was performed using the Powheg Box Res generator and OpenLoops [53–56], with the NNPDF3.0nlo nf4 [57] parton distribution function (PDF) set and Pythia 8.230 [51] with the A14 set

of tuned parameters [58] for the simulation of the parton shower (PS) and hadronisation. Given that the production rate of $t\bar{t}$ with additional b-jets was observed to be underestimated by the current predictions [59, 60], the normalisation of the $t\bar{t}+\geq 1b$ background is determined from the analysed data without prior constraints. The $t\bar{t}+\geq 1c$ and $t\bar{t}+$light backgrounds are modelled from a subset of an inclusive $t\bar{t}+$jets sample generated at NLO in QCD using Powheg Box v2 [61–64] as the ME generator interfaced with Pythia 8.230 for the PS and hadronisation. This inclusive $t\bar{t}+$jets sample is generated with the five-flavour scheme, where c- and b-quarks not originating from a top-quark decay are assumed to be massless. Due to limited knowledge regarding $t\bar{t}+\geq 1c$ production, an additional 100% uncertainty is included in its normalisation. Additionally, a prior uncertainty of 6% is assigned to the inclusive $t\bar{t}+$jets production cross-sections according to the predicted inclusive $t\bar{t}$ production cross-section at NNLO+NNLL [65–71]. Other background processes include the production of $W+$jets, $Z+$jets, $t\bar{t}W$, $t\bar{t}Z$, tZq, tWZ, $t\bar{t}t\bar{t}$ and $WW/WZ/ZZ$ events. These are all subdominant and modelled from simulation as detailed in Ref. [29]. A small fraction of events contain misidentified leptons or leptons originating from the decay of heavy-flavour hadrons. The contribution from these events is found to be negligible in the $\ell+$jets channel. In the dilepton channel, this small contribution is modelled using a simulation.

The signal processes, $t\bar{t}H$ and tH, are simulated with different values of α and κ_t'. All other parameters were fixed to their SM values, including the $H\to b\bar{b}$ branching ratio. The alternative scenarios were simulated using the NLO Higgs Characterisation [30, 72] model implemented in MadGraph5_aMC@NLO with FeynRules [73, 74]. With a few exceptions, all signal samples were generated using the MadGraph5_aMC@NLO 2.6.2 [75] generator at NLO in QCD using the five-flavour scheme with the NNPDF3.0nnlo PDF set, interfaced with Pythia 8.230 with the A14 set of tune parameters for PS and hadronisation. The SM $t\bar{t}H$ events were simulated using MadGraph5_aMC@NLO 2.6.0 . The renormalisation and factorisation scales were set to $\sqrt[3]{m_{\mathrm{T}}(t)\cdot m_{\mathrm{T}}(\bar{t})\cdot m_{\mathrm{T}}(H)}$, where $m_{\mathrm{T}}=\sqrt{m^2+p_{\mathrm{T}}^2}$ is the transverse mass of a particle. The cross-section is normalised to 507 fb from the fixed-order calculation including NLO QCD and electroweak corrections, with an uncertainty of 3.6% from variations in PDF and α_{s} and 9.2% due to variations of the renormalisation and factorisation scales [30, 76–80]. A K-factor of 1.1 is derived by taking the ratio of the cross-section from the fixed-order calculation to that from MadGraph5_aMC@NLO, and is applied to all $t\bar{t}H$ samples with different values of α and κ_t'. For the tH signal, two subprocesses, $tHjb$ and tWH, are considered. The $tHjb$ (tWH) events were generated in the four(five)-flavour scheme using the NNPDF3.0nnlo nf4 (NNPDF3.0nnlo) PDF set [57], with the renormalisation and factorisation scales set to the generator's default. The cross-sections for the $tHjb$ and tWH samples are obtained directly from MadGraph5_aMC@NLO. In the SM scenario, the cross-section for $tHjb$ and tWH are 60.1 fb and 16.7 fb, respectively. Variations of the renormalisation and factorisation scales, including the consideration of the flavour scheme choice for the $tHjb$ process, contribute 15% and 6.7% to the uncertainty of the cross-sections of $tHjb$ and tWH respectively. Similarly, variations of the PDFs and α_{s} result in a 3.7% and 6.3% uncertainty in the $tHjb$ and tWH cross-sections, respectively. A diagram removal scheme [81] is applied in the simulation of the tWH events in order to remove diagrams already included in the $t\bar{t}H$ simulation.

The yields of $t\bar{t}H$ and tH signals are parameterised as a function of the model parameters by smoothly interpolating between generated MC samples with varying α and κ_t'. The parameterisation is performed in each analysis bin. Two $t\bar{t}H$ samples with alternative values of α were generated, corresponding to a pure CP-odd interaction ($\alpha=90^\circ$) and maximal CP-odd/CP-even mixing ($\alpha=45^\circ$). The $t\bar{t}H$ yields, $N_{t\bar{t}H}(\kappa_t',\alpha)$, are parameterised using the SM sample and the pure CP-odd sample as $\kappa_t'^2 c_\alpha^2 N_{CP\text{-even}}+\kappa_t'^2 s_\alpha^2 N_{CP\text{-odd}}$, where $c_\alpha=\cos\alpha$, $s_\alpha=\sin\alpha$, and $N_{CP\text{-even}}$ and $N_{CP\text{-odd}}$ are the expected yields predicted by the SM and the CP-odd $t\bar{t}H$ simulations, respectively. This was verified to be a good approximation using the maximal

mixing sample ($\alpha = 45°$). In the case of tH, the interference between diagrams with CP-even and CP-odd $t-H$ and SM $W-H$ couplings are considered in the parameterisation, assuming contributions from lowest order diagrams of $tHjb$ and tWH processes. The signal yield in each analysis bin is parameterised as $N_{tH}(\kappa_t', \alpha) = A\kappa_t'^2 c_\alpha^2 + B\kappa_t'^2 s_\alpha^2 + C\kappa_t' c_\alpha + D\kappa_t' s_\alpha + E\kappa_t'^2 c_\alpha s_\alpha + F$. Coefficients A-F are derived separately for each analysis bin, by fitting to the yields predicted by multiple simulated samples with varying κ_t' and α. The terms with c_α^2 and s_α^2 correspond to the contribution from CP-even and CP-odd t-H coupling, respectively. The terms at the first order of c_α and s_α account for potential interference effects between CP-even and CP-odd t-H coupling and SM W-H coupling contributions. The term F represents the contribution from only the SM W-H coupling. Ten samples generated with different values of α and κ_t' in addition to the SM tH sample are used for the parameterisation. These samples include: samples where $\kappa_t' = 1$ and α is set between 15° to 90° in steps of 15°, samples with κ_t' = -1, 0.5, and 2 where $\alpha = 0$ and an additional sample with $\alpha = 45°$and $\kappa_t' = 2$. Uncertainties due to limited number of MC events in these simulated samples are considered when performing the parameterisation fit in each bin. Good closure was observed: the largest χ^2 per degree of freedom was 0.19 in any given bin. Uncertainties pertaining to the parameterisation of either signal were found to have a negligible impact on the measured values of α and κ_t'.

5 Analysis strategy

In order to optimise the analysis sensitivity, events satisfying the preselection criteria are categorised into orthogonal regions in two steps. In the first step, control regions (CR) and training regions (TR) are defined using requirements on jet multiplicity, b-tagging and large-R jets. The TRs are defined according to the expected numbers of objects from the decay of the signal events, whilst the CRs with lower object multiplicities are signal depleted. The TRs broadly contain the signals and are used to train various multivariate algorithms (MVA). Dedicated observables are constructed in the TRs to enhance sensitivity to the top-Higgs Yukawa CP coupling. In the second step, MVAs are used to divide the TRs into signal regions (SR) and additional CRs with relatively high and low signal purity, respectively. Given the small contribution expected from tH events, the categorisation, MVAs and CP-sensitive observables are optimised for the $t\bar{t}H$ signal. All regions labelled CR and SR are simultaneously fit to the data using either specific observables or simple yields as specified below. Both steps are described in detail below.

The first step of categorisation adopts a strategy similar to that described in Ref. [29], devised to separate the SM signal from the various backgrounds. A 'boosted' region, labelled as $\mathrm{TR}_{\mathrm{boosted}}$, is firstly defined in the ℓ+jets channel by requiring the presence of a high-p_{T} Higgs boson candidate which is identified using a deep neural network (DNN). The DNN is trained to identify the boosted Higgs boson candidates from among large-R jets with $p_{\mathrm{T}} > 300$ GeV [29]. A mixture of constituent jet masses, pseudo-continuous b-tagging scores and jet substructure observables [82] are utilised as inputs for the training. Events failing this DNN selection defining the $\mathrm{TR}_{\mathrm{boosted}}$ region are categorised into CRs and TRs according to the number of jets (j) and various b-tagging (b) requirements. Events in the TRs are required to have at least the number of jets and b-tagged jets expected from the final state of the $t\bar{t}H$ signal. This results in four statistically independent regions in the dilepton channel, named $\mathrm{CR}^{3j,3b}_{\mathrm{hi}}$, $\mathrm{CR}^{\geq 4j,3b}_{\mathrm{lo}}$, $\mathrm{CR}^{\geq 4j,3b}_{\mathrm{hi}}$ and $\mathrm{TR}^{\geq 4j,\geq 4b}$, and three regions in the ℓ+jets channel, named $\mathrm{CR}^{5j,\geq 4b}_{\mathrm{lo}}$, $\mathrm{CR}^{5j,\geq 4b}_{\mathrm{hi}}$ and $\mathrm{TR}^{\geq 6j,\geq 4b}$. The yields of these regions enter the fit. The requirements used to define all CRs and TRs are summarised in Table 1. Regions labelled with 'hi' ('lo') have relatively higher (lower) fractions of events with true b-jets not from top-quark decays, and are selected with tight (loose) b-tagging requirements. The average ΔR

separation between b-jets ($\Delta R_{bb}^{\text{avg}}$) is used as the observable which enters the fit for $\text{CR}_{\text{lo}}^{5j,\geq 4b}$ and $\text{CR}_{\text{hi}}^{5j,\geq 4b}$ regions as it better constrains the shape of the backgrounds. All mentioned CRs have different fractions of $t\bar{t}$ + light, $t\bar{t}$ + $\geq 1c$ and $t\bar{t}$ + $\geq 1b$ events and this helps to constrain the systematic uncertainties in each of these components.

Table 1: Definition of the CRs and TRs according to the number of jets and b-tagged jets using different b-tagging selection criteria, and the number of boosted Higgs boson candidates. For CRs, the bottom row indicates the observables used in the fit to data in the corresponding regions. For the $\text{TR}_{\text{boosted}}$ region, the b-tagged jets flagged with † are not constituents of the boosted Higgs boson candidate. Events must pass $N_{b\text{-tag}}$ requirements for each b-tagging selection criteria.

Region	Dilepton				ℓ+jets			
	$\text{TR}^{\geq 4j,\geq 4b}$	$\text{CR}_{\text{hi}}^{\geq 4j,3b}$	$\text{CR}_{\text{lo}}^{\geq 4j,3b}$	$\text{CR}_{\text{hi}}^{3j,3b}$	$\text{TR}^{\geq 6j,\geq 4b}$	$\text{CR}_{\text{hi}}^{5j,\geq 4b}$	$\text{CR}_{\text{lo}}^{5j,\geq 4b}$	$\text{TR}_{\text{boosted}}$
N_{jets}	≥ 4			$= 3$	≥ 6	$= 5$		≥ 4
$N_{b\text{-tag}}$ @85%	–				≥ 4			
$N_{b\text{-tag}}$ @77%	–				–			$\geq 2^{\dagger}$
$N_{b\text{-tag}}$ @70%	≥ 4	$= 3$			≥ 4			–
$N_{b\text{-tag}}$ @60%	–	$= 3$	< 3	$= 3$	–	≥ 4	< 4	–
$N_{\text{boosted cand.}}$	–				0			≥ 1
Fit observable	–	Yield			–	$\Delta R_{bb}^{\text{avg}}$		–

In the TRs, two sets of boosted decision trees (BDT) are trained: reconstruction BDTs and classification BDTs. The former is trained to assign jets as coming from the decay of the Higgs boson or top quarks in $t\bar{t}H$ events, while the latter is trained to discriminate the $t\bar{t}H$ signal against the backgrounds. Both the reconstruction BDTs and the classification BDTs are trained using simulated SM $t\bar{t}H$ events. It was tested that their performance is equally good for a pure CP-odd signal. For both the reconstruction and classification BDTs, the training procedures are performed independently for each TR and are identical to those used in Ref. [29]. The reconstruction BDTs are trained to classify the correct combinations of jet assignments from random ones. In order to reconstruct the top-quark and Higgs boson candidates, for each event, all possible permutations of jet assignments are evaluated and the permutation with the highest BDT score is selected. The reconstruction BDTs provide important information that improves the performance of the classification BDTs, whilst allowing for the calculation of observables sensitive to the CP nature of the Yukawa coupling. Classification BDT inputs include reconstruction BDT (DNN in the boosted channel) outputs, pseudo-continuous b-tagging discriminant scores of jets, and kinematic features, such as angular distributions and invariant masses between b-tagged jets. The classification BDTs are used to further refine the TRs to define the final CRs and SRs, as detailed later. The classification BDTs used in $\text{TR}^{\geq 4j,\geq 4b}$, $\text{TR}^{\geq 6j,\geq 4b}$ and $\text{TR}_{\text{boosted}}$ are henceforth denoted by $\text{BDT}^{\geq 4j,\geq 4b}$, $\text{BDT}^{\geq 6j,\geq 4b}$ and $\text{BDT}^{\text{boosted}}$, respectively.

Dedicated CP-sensitive observables are computed in $\text{TR}^{\geq 4j,\geq 4b}$ and $\text{TR}^{\geq 6j,\geq 4b}$ and are used in the fit to determine the CP properties of the top-quark Yukawa coupling. Two CP observables, b_2 and b_4, were found to provide the best discrimination in $\text{TR}^{\geq 6j,\geq 4b}$ of the ℓ+jets channel and $\text{TR}^{\geq 4j,\geq 4b}$ of the dilepton channel, respectively. They are defined as:

$$b_2 = \frac{(\vec{p}_1 \times \hat{z}) \cdot (\vec{p}_2 \times \hat{z})}{|\vec{p}_1||\vec{p}_2|}, \text{ and } b_4 = \frac{(\vec{p}_1 \cdot \hat{z})(\vec{p}_2 \cdot \hat{z})}{|\vec{p}_1||\vec{p}_2|},$$

where $\vec{p}_i$ with $i = 1, 2$ are the momentum three-vectors of the two top quarks in the events and $\hat{z}$ is a unit vector in the direction of the beamline and defines the z-axis [15]. The b_4 observable exploits the enhanced production of top quarks travelling in opposite longitudinal directions and closer to the beamline in CP-odd $t\bar{t}H$ production. The observable b_2 relies simultaneously on the smaller azimuthal separation of top quarks and on their larger longitudinal fraction of momentum in CP-odd $t\bar{t}H$ production. The calculation of b_2 is performed in the $t\bar{t}H$ rest frame [28], which enhances the discrimination power.

Computation of b_2 and b_4 requires the full reconstruction of both top quarks and the Higgs boson. However, the reconstruction BDTs only resolve the hadronic part of the $t\bar{t}H$ system. In the ℓ+jets channel, the missing transverse momentum is used as a proxy for the p_{T} of the undetected neutrino from the semileptonically decaying top quark. The z component of the neutrino four-momentum is obtained from a quadratic equation constructed from the lepton four-momentum and the missing transverse momentum, using as a constraint the leptonic W boson's mass, assumed to be its on-shell value. Both solutions of the quadratic equation are used to reconstruct the top-quark mass, and the one yielding a mass closer to 172.5 GeV is chosen. In the case of a negative determinant, a solution is obtained by setting the determinant to zero. In the dilepton channel, the neutrino weighting technique is used to determine the four momenta of the two neutrinos [83, 84]. Neutrino weighting provides a solution for reconstructing the $t\bar{t}$ pair for 68% of the events in $\mathrm{TR}^{\geq 4j,\geq 4b}$.

In contrast to the $\mathrm{TR}^{\geq 4j,\geq 4b}$ and $\mathrm{TR}^{\geq 6j,\geq 4b}$ regions, the CP-odd signals are strongly enhanced in comparison with the CP-even signals in the $\mathrm{TR}_{\mathrm{boosted}}$ region. The yields of $t\bar{t}H$ with pure CP-even and CP-odd couplings are approximately equal in the $\mathrm{TR}_{\mathrm{boosted}}$ region. Additionally, the yield of the tH signal with a pure CP-odd coupling is comparable to the $t\bar{t}H$ signal yield. A CP-odd signal is expected to be 50% larger than a CP-even signal in this region. Given the substantial sensitivity provided by the yield in this region, the distribution of the classification BDT ($\mathrm{BDT}^{\mathrm{boosted}}$) is used instead of a dedicated CP-sensitive observable.

In the second step of the categorisation, TRs are further refined to CRs and SRs according to the output of the reconstruction and classification BDTs. A summary of the selections used to define the regions is detailed in Table 2. In $\mathrm{TR}_{\mathrm{boosted}}$, events below a classification BDT score of –0.05 are discarded to reduce contamination of $t\bar{t}$ + light events. $\mathrm{TR}^{\geq 4j,\geq 4b}$ and $\mathrm{TR}^{\geq 6j,\geq 4b}$ are further categorised, each into three regions, according to the classification BDT score. The resulting regions have similar background compositions but different expected signal-to-background ratios (S/B). The BDT thresholds are determined by optimising the sensitivity to the SM $t\bar{t}H$ signal. The three regions (one in ℓ+jets and two in dilepton) with an $S/B > 7\%$ are used as SRs. The remaining three regions (two in ℓ+jets and one in dilepton) are used as additional CRs to constrain the modelling of the CP observables in the backgrounds events. The highest S/B in the resulting SRs is 22% (10%) for a pure CP-even (CP-odd) signal. For $\mathrm{SR}^{\geq 4j,\geq 4b}$ in the dilepton channel, b_4 cannot be calculated for events where the neutrino weighting fails to provide a solution. These events are categorised as an additional region, $\mathrm{CR}^{\geq 4j,\geq 4b}_{\text{no-reco}}$, where the difference in η between the two leptons, $\Delta\eta_{\ell\ell}$, is used as a CP-sensitive observable instead [19].

6 Systematic uncertainties

Systematic uncertainties are assessed for three main sources: theoretical modelling of the signal processes, background modelling which is dominated by the uncertainties in the $t\bar{t}+\geq 1b$ background and experimental sources involving the (mis)identification rates and energy calibration of leptons, jets, b-jets and missing transverse momentum. Uncertainties accounting for the limited number of events in all simulated samples

Table 2: Summary of the selections used to define SRs and CRs from the TRs, based on the classification BDT score. In the boosted region, the selection requirement is applied and rejected events are removed entirely from further analysis. In the dilepton channel, events with failed reconstruction due to absence of a real solution from the neutrino weighting are categorised into an additional region known as $\mathrm{CR}_{\text{no-reco}}^{\geq 4j,\geq 4b}$. The fitted discriminating variable in each region is indicated in the last column.

Channel (TR)	Final SRs and CRs	Classification BDT selection	Fitted observable
Dilepton ($\mathrm{TR}^{\geq 4j,\geq 4b}$)	$\mathrm{CR}_{\text{no-reco}}^{\geq 4j,\geq 4b}$	–	$\Delta\eta_{\ell\ell}$
	$\mathrm{CR}^{\geq 4j,\geq 4b}$	$\mathrm{BDT}^{\geq 4j,\geq 4b} \in [-1, -0.086)$	b_4
	$\mathrm{SR}_1^{\geq 4j,\geq 4b}$	$\mathrm{BDT}^{\geq 4j,\geq 4b} \in [-0.086, 0.186)$	b_4
	$\mathrm{SR}_2^{\geq 4j,\geq 4b}$	$\mathrm{BDT}^{\geq 4j,\geq 4b} \in [0.186, 1]$	b_4
ℓ+jets ($\mathrm{TR}^{\geq 6j,\geq 4b}$)	$\mathrm{CR}_1^{\geq 6j,\geq 4b}$	$\mathrm{BDT}^{\geq 6j,\geq 4b} \in [-1, -0.128)$	b_2
	$\mathrm{CR}_2^{\geq 6j,\geq 4b}$	$\mathrm{BDT}^{\geq 6j,\geq 4b} \in [-0.128, 0.249)$	b_2
	$\mathrm{SR}^{\geq 6j,\geq 4b}$	$\mathrm{BDT}^{\geq 6j,\geq 4b} \in [0.249, 1]$	b_2
ℓ+jets ($\mathrm{TR}_{\text{boosted}}$)	$\mathrm{SR}_{\text{boosted}}$	$\mathrm{BDT}^{\text{boosted}} \in [-0.05, 1]$	$\mathrm{BDT}^{\text{boosted}}$

are also considered. Systematic variations can affect the overall yields, relative yields between analysis regions and shapes of observables.

Uncertainties associated with the modelling of the $t\bar{t}H$ signals include variations due to initial and final state radiation (ISR and FSR), choice of the NLO matching procedure as well as the PS and hadronisation model. These uncertainties are evaluted using events generated with Powheg Box + Pythia 8 samples, which are produced with the same PDF set and renormalisation and factorisation scales as the nominal MadGraph5_aMC@NLO + Pythia 8 sample, unless otherwise specified. Variations relative to the SM hypothesis are propagated to scenarios with alternative values of α and κ_t'. To estimate the uncertainty related to the amount of partonic ISR, the renormalisation and factorisation scales in the ME and $\alpha_{\mathrm{S}}^{\mathrm{ISR}}$ in the PS are varied simultaneously [85]. The impact of the FSR is evaluated by varying $\alpha_{\mathrm{S}}^{\mathrm{FSR}}$ in the PS. The impact of varying the PS and hadronisation models is estimated by comparing $t\bar{t}H$ samples generated using Powheg Box + Pythia 8.230 with those generated from Powheg Box + Herwig 7.04 [86]. The uncertainty due to the choice of NLO matching procedure is derived by directly comparing the Powheg Box + Pythia 8 sample with the nominal MadGraph5_aMC@NLO + Pythia 8 sample. The uncertainties in the modelling of tH are estimated using the nominal sample generated using MadGraph5_aMC@NLO + Pythia 8. For each tH subprocess ($tHjb$ and tWH), two sources of modelling uncertainty are considered: that associated with the description of PDFs, and the uncertainty due to missing higher-order QCD contributions. The former is estimated from the standard deviation of the expected yields using 100 NNPDF3.0nlo eigenvector PDF sets, in each analysis bin used to build the likelihood function. The latter is estimated by coherently varying μ_{r} and μ_{f} by factors of 0.5 and 2.

The most important uncertainties in the background estimation come from the modelling of the $t\bar{t}+\geq 1b$ background. These uncertainties are designed to account for the choice of NLO matching procedure, PS and hadronisation model as well as the flavour scheme utilised in the $t\bar{t}+\geq 1b$ event generation. An uncertainty in the ME-to-PS matching procedure is assessed by comparing the Powheg Box + Pythia 8 sample with a sample generated using MadGraph5_aMC@NLO + Pythia 8, both in the five-flavour scheme. The variation by comparing these two samples is propagated to the nominal $t\bar{t}+\geq 1b$ sample generated with Powheg Box Res + Pythia 8 in the four-flavour scheme. This uncertainty is treated independently in each

of the dilepton channel, the non-boosted regions in the ℓ+jets channel and the ℓ+jets boosted region. This treatment is found to be important because it provides the fit with enough flexibility to cover the potential background mismodelling. Uncertainties in the choice of the PS model are evaluated by comparing the nominal sample with the one produced with Powheg Box + Herwig 7. These uncertainties are treated in the same way as the uncertainty in the NLO matching procedure. An additional source of systematic uncertainty is introduced to address the choice of flavour scheme used for the generation of the $t\bar{t}+\geq 1b$ events. It is evaluated by comparing the nominal sample, generated in the four-flavour scheme using Powheg + Pythia 8, with that produced in the five-flavour scheme reweighted to remove differences in scale settings. Uncertainties in ISR and FSR are estimated using the same procedure as used for the $t\bar{t}H$ signals. An uncertainty due to differences in relative fraction of $t\bar{t}+1b$ and $t\bar{t}+\geq 2b$ subcomponents from different MC predictions is also considered. Other uncertainties in $t\bar{t}+\geq 1b$ and uncertainties in other background components are treated identically to the procedure described in Ref. [29].

Aside from the modelling uncertainties described above, experimental uncertainties are also considered. These arise from the modelling of trigger, reconstruction, identification and isolation efficiencies, as well as the calibration of energy and momentum scales for all physics objects, including electrons, muons, jets, b-tagged jets and $E_{\mathrm{T}}^{\mathrm{miss}}$. Uncertainties in the measured integrated luminosity and in the modelling of additional pp collisions are included.

7 Results and conclusion

A binned profile likelihood fit is performed including all analysis regions simultaneously in order to determine the α and κ_t' parameters. The likelihood function, $\mathcal{L}(\alpha, \kappa_t', \boldsymbol{\theta})$, is constructed as the product of Poisson terms, with each term corresponding to an analysis bin. The value of the likelihood varies according to the expected signal yields, as a function of α and κ_t', and background yields of the analysis bins, as well as $\boldsymbol{\theta}$, representing the nuisance parameters encoding the effects of the systematic uncertainties and a single parameter controlling the normalisation of the $t\bar{t}+\geq 1b$ background. The nuisance parameters are constrained with Gaussian or log-normal functions. The normalisation of the $t\bar{t}+\geq 1b$ background is controlled by an unconstrained parameter $k_{t\bar{t}+b}$. A profile likelihood ratio is used as the test statistic, following Ref. [87]. By scanning the value of the test statistic in grid points in κ_t' and α, two-dimensional exclusion contours in the (κ_t', α) plane are obtained.

Figure 1 compares the observed yield of data in each analysis region with that expected after the fit to data (post-fit). The expected yields for pure CP-even and CP-odd signals, normalised to the total data yields, are overlaid and shown with dashed lines in the top panels. These illustrate the signal-to-background separation provided by the classification BDTs. In the middle panel, the best-fit model is compared with the data by showing ratios of its value to the post-fit background prediction. The post-fit model agrees well with the observed data. In addition, the expected S/B for pure CP-even and CP-odd signals are shown for both $t\bar{t}H$ and tH. The post-fit yields for all backgrounds and the signals are summarised in Tables 3 and 4 for the ℓ+jets and dilepton channels, respectively. The expected yields of pure CP-even and CP-odd signals are compared with the post-fit yields. In all fitted regions, the best-fit signal yields are lower than their SM predictions. The fitted value $k_{t\bar{t}+b}$ is $1.30^{+0.09}_{-0.08}$, consistent with the value measured in Ref. [29]. Figure 2 shows the distributions of the fitted observables in the four SRs. The post-fit predictions are in agreement with data. Goodness-of-fit was evaluated using a likelihood ratio test, comparing the likelihood value from the nominal fit with the one obtained from a saturated model built with one free-floating normalisation factor for each fitted bin [88]. The probability that the post-fit prediction is compatible with the observed

data is 80%. The pure CP-even and CP-odd signals are shown overlaid and normalised to the data yield to indicate the kinematic discrimination of the b_2 and b_4 observables.

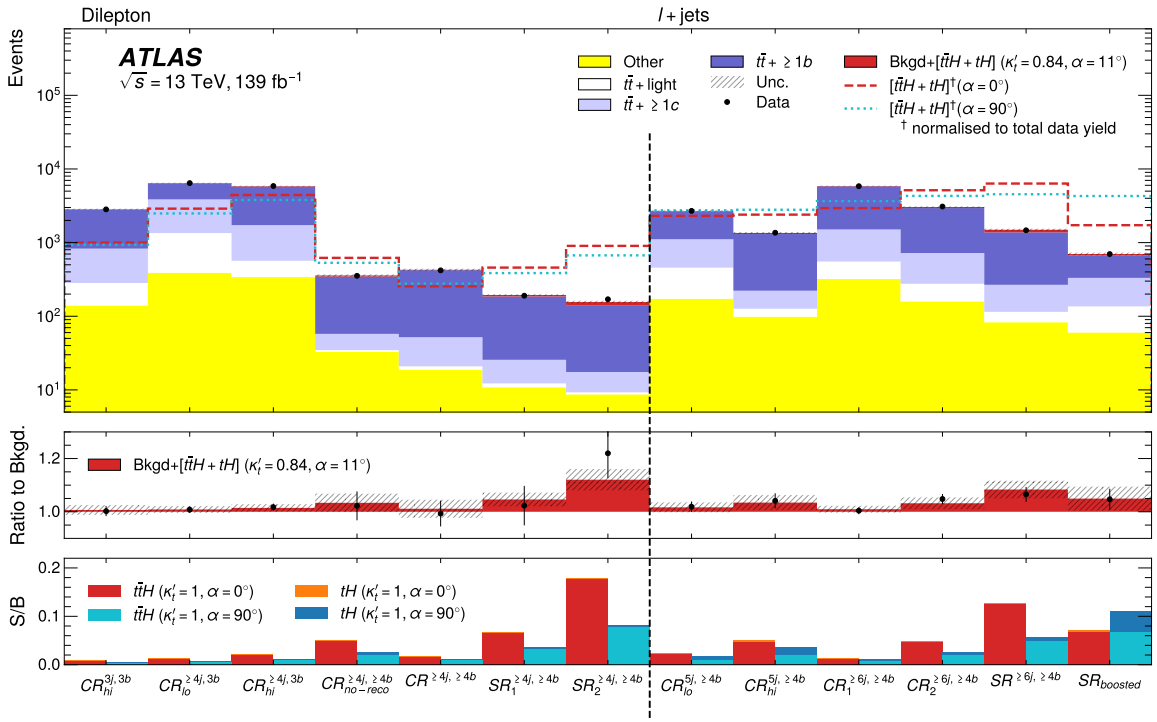

Figure 1: Yields calculated following a fit with κ_t' and α as free parameters, compared to the observed data in all analysis regions. The different backgrounds and the signal are shown in coloured stack. The background component labelled "other" corresponds to the production of W+ jets, Z+ jets, $t\bar{t}W$, $t\bar{t}Z$, tZq, tWZ, $t\bar{t}t\bar{t}$ and $WW/WZ/ZZ$ events, as in Ref. [29]. The dashed and dotted lines show the sum of $t\bar{t}H + tH$ signals for pure CP-even and CP-odd hypotheses normalised to the total data yields including all regions. The hashed area around the prediction illustrates the total post-fit uncertainties. In the middle panel, the best-fit model is compared with the data by showing ratios of its value to the post-fit background prediction. The histogram represents the total post-fit model including the best-fit signals. The hashed band represents the total post-fit uncertainty as a ratio to the background. In the bottom panel, the S/B is shown for pure CP-even and CP-odd signals, separately. The histograms are shown as a stack of $t\bar{t}H$ and tH.

The best-fit values and the exclusion contours in α and κ_t' are displayed in Figure 3 in the $(\kappa_t' \cos\alpha, \kappa_t' \sin\alpha)$ plane. The best-fit value for the CP mixing angle α is $11^{\circ}{}^{+56^{\circ}}_{-77^{\circ}}$ and overall coupling strength κ_t' is $0.84^{+0.30}_{-0.46}$, which are in agreement with the SM expectations of $\alpha = 0^{\circ}$ and $\kappa_t' = 1$. The data disfavour the pure CP-odd hypothesis with a 1.2 σ significance. The significance of the observed $t\bar{t}H$ and tH signals over the background prediction is 1.3 σ. The compatibility of this analysis with the $t\bar{t}H$ cross-section measurement [29] was tested with the same parameter of interest: a single free-floating signal strength, $\mu_{t\bar{t}H}$, controlling the normalisation of $t\bar{t}H$ production in the SM scenario. The tH process was fixed to its SM prediction with an identical systematic model. The compatibility is tested using the bootstrap technique. The difference in the measured $\mu_{t\bar{t}H}$ is sampled by fitting to toy datasets generated by varying the event weights entering the Asimov dataset according to the Poisson fluctuations expected in data. The measured values of $\mu_{t\bar{t}H}$ were found to be compatible within one standard deviation, when accounting for the statistical correlations between the two measurements.

The impact of a group of systematic uncertainties on α (κ_t') is assessed by fixing the nuisance parameters to their best fit values and subtracting the subsequent α (κ_t') uncertainty in quadrature from the total α (κ_t')

Table 3: The observed data yields and the expected signal and background yields in the ℓ+jets channel. The expected yields of pure CP-even and CP-odd $t\bar{t}H$ and tH signals, with $\kappa_t' = 1$, are shown at the top of the table. The uncertainties in the pure CP-even and CP-odd $t\bar{t}H$ and tH signals are the total uncertainties before fitting to data. Below that are shown the post-fit $t\bar{t}H$ and tH yields, corresponding to $\kappa_t' = 0.84$ and $\alpha = 11°$. The following seven rows show the yields and uncertainties of individual background sources, where "other" corresponds to W+ jets, Z+ jets, $t\bar{t}W$, $t\bar{t}Z$, tZq, tWZ, $t\bar{t}t\bar{t}$ and $WW/WZ/ZZ$ events, as in Ref. [29]. The row labelled 'Total' represents the total signal plus background post-fit yields. The uncertainties in the post-fit yields are evaluated from the post-fit nuisance parameters as well as the post-fit uncertainties in the fitted free parameters (α and κ_t' for the signals and $k_{t\bar{t}+b}$ for the $t\bar{t}$ + ≥1b background) that affect the corresponding processes. The correlations amongst all fitted parameters are taken into account. Due to these correlations the uncertainties on the total yields do not correspond to the quadrature sum of uncertainties of individual signals and backgrounds.

	$\mathrm{CR}_{\mathrm{lo}}^{5j,\geq 4b}$	$\mathrm{CR}_{\mathrm{hi}}^{5j,\geq 4b}$	$\mathrm{CR}_{1}^{\geq 6j,\geq 4b}$	$\mathrm{CR}_{2}^{\geq 6j,\geq 4b}$	$\mathrm{SR}^{\geq 6j,\geq 4b}$	$\mathrm{SR}_{\mathrm{boosted}}$
$t\bar{t}H$ $(1, 0°)$	60 ± 9	63 ± 10	78 ± 11	139 ± 18	173 ± 26	46 ± 6
$tH(1, 0°)$	3.5 ± 0.5	3.8 ± 0.6	3.3 ± 0.6	2.3 ± 0.6	1.3 ± 0.4	1.9 ± 0.4
$t\bar{t}H$ $(1, 90°)$	28 ± 6	28 ± 6	45 ± 11	61 ± 12	68 ± 16	45 ± 6
$tH(1, 90°)$	19.0 ± 2.8	19.4 ± 3.1	17.4 ± 3.1	13.1 ± 3.5	10 ± 4	29 ± 6
$t\bar{t}H$ $(0.84, 11°)$	40 ± 30	41 ± 31	50 ± 40	90 ± 70	110 ± 80	30 ± 22
tH $(0.84, 11°)$	3 ± 4	3.9 ± 1.9	3.1 ± 1.9	1.9 ± 0.8	1.3 ± 1.7	3 ± 5
$t\bar{t}$+ ≥ 1b	1530 ± 80	1090 ± 60	4300 ± 120	2220 ± 120	1110 ± 110	335 ± 30
$t\bar{t}$+ ≥ 1c	650 ± 50	96 ± 11	950 ± 80	450 ± 40	153 ± 15	196 ± 22
$t\bar{t}$+ light	280 ± 40	28 ± 8	230 ± 60	117 ± 26	32 ± 11	76 ± 15
Other	173 ± 30	99 ± 20	320 ± 50	159 ± 21	83 ± 11	60 ± 11
Total	2690 ± 50	1350 ± 40	5870 ± 80	3040 ± 70	1500 ± 50	701 ± 31
Data	2696	1363	5837	3090	1470	699

uncertainty. The uncertainty in the measured value of α is dominated by $t\bar{t}$ + ≥1b modelling uncertainties which contribute $^{+37°}_{-51°}$ to the overall uncertainty. This is driven by: the NLO matching procedure between the ME and PS; PS and hadronisation; and the choice of flavour scheme. These uncertainties contribute $^{+22°}_{-33°}$, $^{+16°}_{-24°}$ and $^{+23°}_{-37°}$, respectively. Smaller effects from the $t\bar{t}$ + ≥1b modelling originate from the ISR uncertainty and the relative fractions of $t\bar{t}$ + ≥2b and $t\bar{t}$ + 1b, contributing $^{+14°}_{-24°}$ and $^{+14°}_{-21°}$. The $t\bar{t}$ + ≥1c modelling uncertainties contribute only $^{+6.6°}_{-11°}$ to the uncertainty in α. The 100% $t\bar{t}$ + ≥1c normalisation uncertainty is constrained to 50% with a pull of 0.6 σ, and has negligible impact on the fitted α and κ_t'. Through a correlation with α, the measured κ_t' contributes $^{+17°}_{-33°}$ to the α uncertainty. Experimental uncertainties are smaller than the $t\bar{t}$ + ≥1b modelling uncertainties. The statistical uncertainty is $^{+32°}_{-49°}$.

Table 4: The observed data yields and the expected signal and background yields in the dilepton channel. The expected yields of pure CP-even and CP-odd $t\bar{t}H$ and tH signals, with $\kappa_t' = 1$, are shown at the top of the table. The uncertainties in the pure CP-even and CP-odd $t\bar{t}H$ and tH signals are the total uncertainties before fitting to data. Below that are shown the post-fit $t\bar{t}H$ and tH yields, corresponding to $\kappa_t' = 0.84$ and $\alpha = 11^\circ$. The following seven rows show the yields and uncertainties of individual background sources, where "other" corresponds to W+ jets, Z+ jets, $t\bar{t}W$, $t\bar{t}Z$, tZq, tWZ, $t\bar{t}t\bar{t}$ and $WW/WZ/ZZ$ events, as in Ref. [29]. The row labelled 'Total' represents the total signal plus background post-fit yields. The uncertainties in the post-fit yields are evaluated from the post-fit nuisance parameters as well as the post-fit uncertainties in the fitted free parameters (α and κ_t' for the signals and $k_{t\bar{t}+b}$ for the $t\bar{t}$ + $\geq 1b$ background) that affect the corresponding processes. The correlations amongst all fitted parameters are taken into account. Due to these correlations the uncertainties in the total yields do not correspond to the quadrature sum of uncertainties of individual signals and backgrounds.

	$\mathrm{CR}_{\mathrm{hi}}^{3j,3b}$	$\mathrm{CR}_{\mathrm{lo}}^{\geq 4j,3b}$	$\mathrm{CR}_{\mathrm{hi}}^{\geq 4j,3b}$	$\mathrm{CR}_{\text{no-reco}}^{\geq 4j,\geq 4b}$	$\mathrm{CR}^{\geq 4j,\geq 4b}$	$\mathrm{SR}_1^{\geq 4j,\geq 4b}$	$\mathrm{SR}_2^{\geq 4j,\geq 4b}$
$t\bar{t}H$ $(1, 0^\circ)$	26 ± 4	79 ± 8	120 ± 12	16.9 ± 2.1	6.9 ± 1.1	12.5 ± 1.5	24.8 ± 2.9
$tH(1, 0^\circ)$	1.12 ± 0.13	0.90 ± 0.13	1.74 ± 0.20	0.19 ± 0.08	0.087 ± 0.035	0.100 ± 0.033	0.09 ± 0.06
$t\bar{t}H$ $(1, 90^\circ)$	10.6 ± 1.6	35.6 ± 3.5	54 ± 5	7.2 ± 0.9	4.3 ± 0.6	6.1 ± 0.7	10.9 ± 1.3
$tH(1, 90^\circ)$	5.4 ± 0.6	7.0 ± 1.0	10.7 ± 1.2	1.8 ± 0.8	0.48 ± 0.19	0.48 ± 0.16	0.5 ± 0.4
$t\bar{t}H$ $(0.84, 11^\circ)$	18 ± 14	50 ± 40	80 ± 60	11 ± 9	4.7 ± 3.4	8 ± 6	17 ± 12
tH $(0.84, 11^\circ)$	0.9 ± 0.5	1.0 ± 1.9	1.5 ± 1.3	0.17 ± 0.16	0.068 ± 0.016	0.08 ± 0.14	0.07 ± 0.09
$t\bar{t}$+ $\geq 1b$	1990 ± 80	2520 ± 110	4040 ± 130	288 ± 15	371 ± 16	160 ± 8	122 ± 11
$t\bar{t}$+ $\geq 1c$	550 ± 50	2510 ± 150	1160 ± 90	23 ± 4	31.1 ± 2.5	13.4 ± 1.6	8.2 ± 1.0
$t\bar{t}$+ light	143 ± 27	960 ± 130	230 ± 40	1.7 ± 0.4	2.3 ± 0.8	1.4 ± 0.8	0.57 ± 0.25
Other	140 ± 11	390 ± 19	340 ± 40	33 ± 8	18.6 ± 2.5	10.9 ± 1.3	8.7 ± 1.0
Total	2840 ± 50	6430 ± 80	5850 ± 80	358 ± 12	428 ± 15	194 ± 5	156 ± 6
Data	2827	6429	5865	354	420	190	170

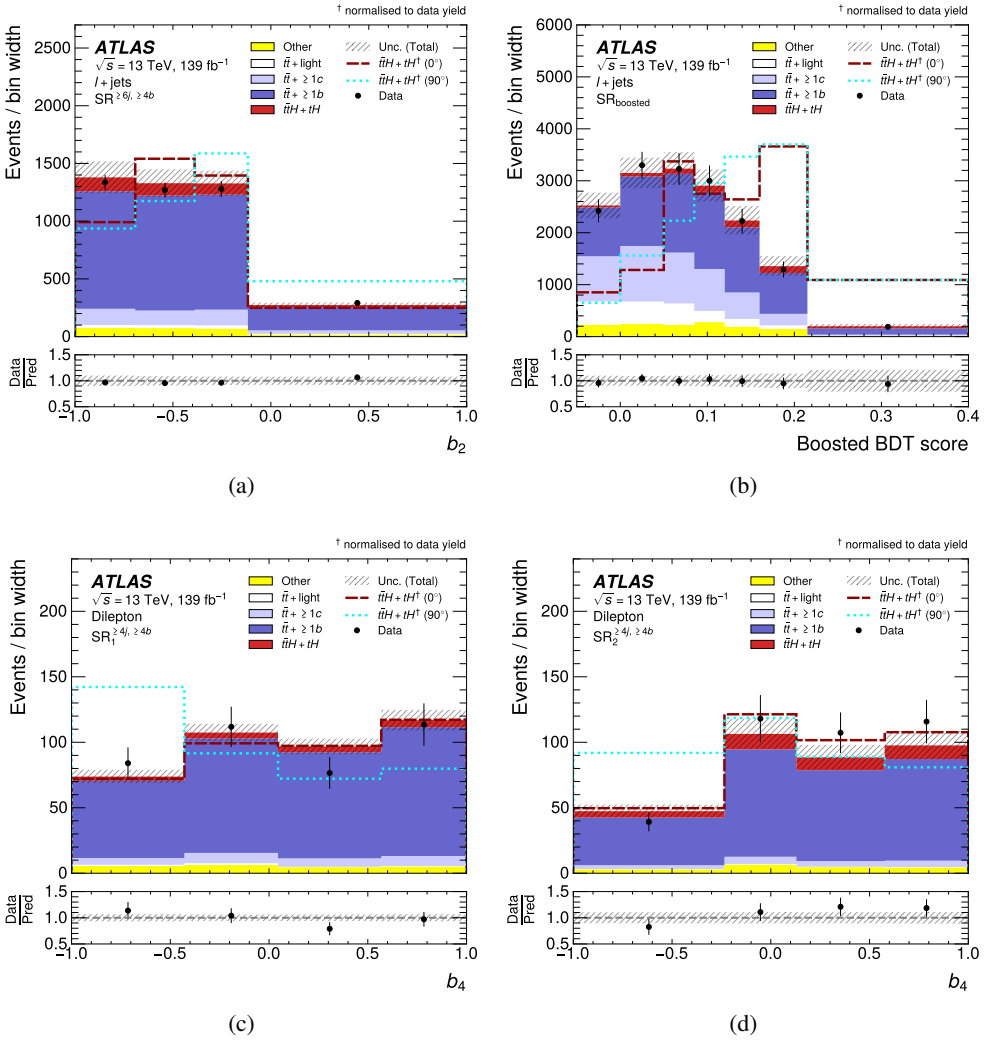

Figure 2: The distributions of the fitted variables in all signal regions. The stacked histograms represent the predictions from a fit of signal and background to data with both κ_t' and α as free parameters. This is compared with data shown with black dots. The solid red histogram shows the best-fit signal with $\alpha = 11^\circ$ and $\kappa_t' = 0.84$. The dashed and dotted lines show $t\bar{t}H + tH$ signal predictions for pure CP-even and CP-odd hypotheses, respectively, normalised to the total data yield per region in order to illustrate the shapes of the signal distribution. The hashed area around the prediction illustrates the total post-fit uncertainties. The lower panel shows the ratio of data to the predicted yields from a fit of signal and background in which κ_t' and α are free parameters.

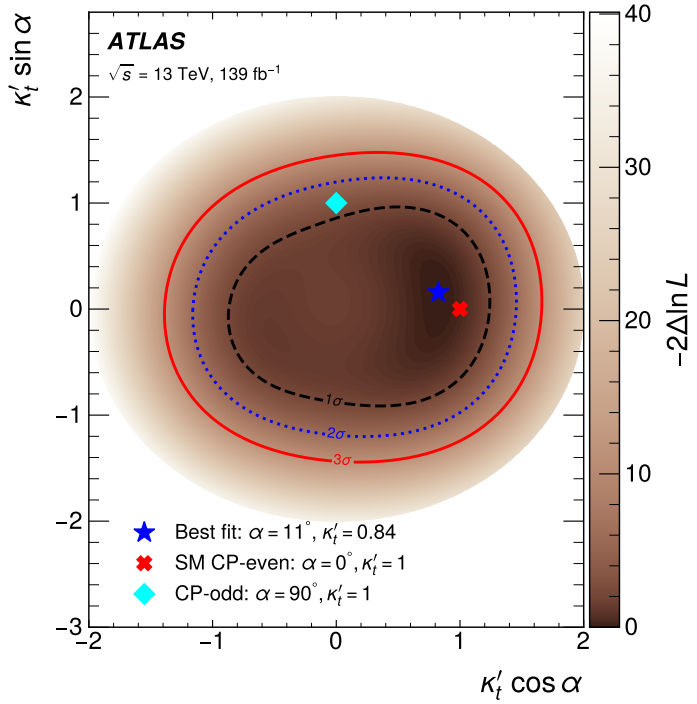

Figure 3: The observed exclusion contours in the $(\kappa_t' \cos\alpha, \kappa_t' \sin\alpha)$ plane. Regions contained in the dashed, dotted and solid lines are compatible with the best-fit results at 1, 2 and 3 σ standard deviations. The cross (diamond) represents the CP-even (CP-odd) with κ_t' =1 and the best-fit result is represented with a pentagram.

In conclusion, the CP properties of the top-quark's Yukawa coupling to the Higgs boson are probed in $t\bar{t}H$ and tH production with $H \to b\bar{b}$ decays, which had not been studied before. Dedicated CP-sensitive variables relying on angular separations between reconstructed top quarks or lepton candidates were used directly. Assuming the SM branching ratio for the Higgs boson decay, the best-fit values of the CP-mixing angle and the overall coupling strength are $\alpha = 11^{\circ}{}^{+52^{\circ}}_{-73^{\circ}}$ and $\kappa_t' = 0.84^{+0.30}_{-0.46}$. These values can be compared with the expected allowed 1 σ range of $\alpha \in [-180^{\circ}, -173^{\circ}] \cup [-50^{\circ}, 52^{\circ}] \cup [171^{\circ}, 180^{\circ}]$ and $\kappa_t' = 1.00^{+0.29}_{-0.27}$ for a CP-even scenario and $\alpha \in [-157^{\circ}, -41^{\circ}] \cup [43^{\circ}, 157^{\circ}]$ and $\kappa_t' = 1.00^{+0.22}_{-0.33}$ for a pure CP-odd scenario.

These results complement previous ATLAS measurements in the $H \to \gamma\gamma$ decay channel and will allow for a future combined measurement of the CP properties of the top-quark Yukawa coupling. Due to the tree-level sensitivity and the high $H \to b\bar{b}$ branching ratio, it can be expected that future measurements in the $t\bar{t}H$ and tH channels will become quite sensitive to the CP properties of the top-quark Yukawa coupling. Additional LHC data and a better theoretical understanding of the $t\bar{t} + \geq 1b$ process will be essential ingredients in order to achieve this sensitivity.

References

[1] ATLAS Collaboration, *Observation of a new particle in the search for the Standard Model Higgs boson with the ATLAS detector at the LHC*, Phys. Lett. B **716** (2012) 1, arXiv: 1207.7214 [hep-ex].

[2] CMS Collaboration, *Observation of a new boson with mass near 125 GeV in pp collisions at $\sqrt{s}$ = 7 and 8 TeV*, JHEP **06** (2013) 081, arXiv: 1303.4571 [hep-ex].

[3] ATLAS Collaboration, *Observation of Higgs boson production in association with a top quark pair at the LHC with the ATLAS detector*, Phys. Lett. B **784** (2018) 173, arXiv: 1806.00425 [hep-ex].

[4] CMS Collaboration, *Observation of $t\bar{t}H$ Production*, Phys. Rev. Lett. **120** (2018) 231801, arXiv: 1804.02610 [hep-ex].

[5] ATLAS Collaboration, *CP Properties of Higgs Boson Interactions with Top Quarks in the $t\bar{t}H$ and tH Processes Using $H \to \gamma\gamma$ with the ATLAS Detector*, Phys. Rev. Lett. **125** (2020) 061802, arXiv: 2004.04545 [hep-ex].

[6] CMS Collaboration, *Measurements of $t\bar{t}H$ Production and the CP Structure of the Yukawa Interaction between the Higgs Boson and Top Quark in the Diphoton Decay Channel*, Phys. Rev. Lett. **125** (2020) 061801, arXiv: 2003.10866 [hep-ex].

[7] D. Fontes, J. C. Romão, R. Santos and J. P. Silva, *Large pseudoscalar Yukawa couplings in the complex 2HDM*, JHEP **2015** (2015) 60, arXiv: 1502.01720v2 [hep-ph].

[8] ATLAS Collaboration, *Search for a CP-odd Higgs boson decaying to Zh in pp collisions at $\sqrt{s}$ = 8 TeV with the ATLAS detector*, Phys. Lett. B **744** (2015) 163, arXiv: 1502.04478 [hep-ex].

[9] ATLAS Collaboration, *Test of CP invariance in vector-boson fusion production of the Higgs boson in the $H \to \tau\tau$ channel in proton–proton collisions at $\sqrt{s}$ = 13 TeV with the ATLAS detector*, Phys. Lett. B **805** (2020) 135426, arXiv: 2002.05315 [hep-ex].

[10] ATLAS Collaboration, *Measurements of Higgs boson properties in the diphoton decay channel with* $36\,fb^{-1}$ *of* pp *collision data at* $\sqrt{s} = 13$ *TeV with the ATLAS detector*, Phys. Rev. D **98** (2018) 052005, arXiv: 1802.04146 [hep-ex].

[11] ATLAS Collaboration, *Measurement of the Higgs boson coupling properties in the* $H \to ZZ^* \to 4\ell$ *decay channel at* $\sqrt{s} = 13$ *TeV with the ATLAS detector*, JHEP **03** (2018) 095, arXiv: 1712.02304 [hep-ex].

[12] CMS Collaboration, *Combined search for anomalous pseudoscalar HVV couplings in* $VH(H \to b\bar{b})$ *production and* $H \to VV$ *decay*, Phys. Lett. B **759** (2016) 672, arXiv: 1602.04305 [hep-ex].

[13] CMS Collaboration, *Constraints on anomalous Higgs boson couplings using production and decay information in the four-lepton final state*, Phys. Lett. B **775** (2017) 1, arXiv: 1707.00541 [hep-ex].

[14] CMS Collaboration, *Measurements of the Higgs boson width and anomalous HVV couplings from on-shell and off-shell production in the four-lepton final state*, Phys. Rev. D **99** (2019) 112003, arXiv: 1901.00174 [hep-ex].

[15] J. F. Gunion and X.-G. He, *Determining the CP Nature of a Neutral Higgs Boson at the CERN Large Hadron Collider*, Phys. Rev. Lett. **76** (1996) 4468, arXiv: hep-ph/9602226.

[16] J. Ellis, D. S. Hwang, K. Sakurai and M. Takeuchi, *Disentangling Higgs-top couplings in associated production*, JHEP **04** (2014) 004, arXiv: 1312.5736 [hep-ph].

[17] X.-G. He, G.-N. Li and Y.-J. Zheng, *Probing Higgs boson CP properties with* $t\bar{t}H$ *at the LHC and the 100 TeV pp collider*, Int. J. Mod. Phys. A **30** (2014) 1550156, arXiv: 1501.00012 [hep-ph].

[18] F. Boudjema, D. Guadagnoli, R. M. Godbole and K. A. Mohan, *Laboratory-frame observables for probing the top-Higgs boson interaction*, Phys. Rev. D **92** (2015) 015019, arXiv: 1501.03157 [hep-ph].

[19] F. Demartin, F. Maltoni, K. Mawatari, B. Page and M. Zaro, *Higgs characterisation at NLO in QCD: CP properties of the top-quark Yukawa interaction*, Eur. Phys. J. C **74** (2014) 3065, arXiv: 1407.5089 [hep-ph].

[20] H. Bahl et al., *Indirect CP probes of the Higgs-top-quark interaction: current LHC constraints and future opportunities*, JHEP **2020** (2020) 127, arXiv: 2007.08542 [hep-ph].

[21] D. Gonçalves, J. H. Kim, K. Kong and Y. Wu, *Direct Higgs-top CP-phase measurement with* $t\bar{t}h$ *at the 14 TeV LHC and 100 TeV FCC*, JHEP **2022** (2022) 158, arXiv: 2108.01083 [hep-ph].

[22] J. Brod, U. Haisch and J. Zupan, *Constraints on CP-violating Higgs couplings to the third generation*, JHEP **11** (2013) 180, arXiv: 1310.1385 [hep-ph].

[23] V. Andreev et al., *Improved limit on the electric dipole moment of the electron*, Nature **562** (2018) 355.

[24] C. Abel et al., *Measurement of the Permanent Electric Dipole Moment of the Neutron*, Phys. Rev. Lett. **124** (8 2020) 081803, arXiv: 2001.11966 [hep-ex].

[25] M. R. Buckley and D. Goncalves, *Boosting the Direct CP Measurement of the Higgs-Top Coupling*, Phys. Rev. Lett. **116** (2016) 091801, arXiv: 1507.07926 [hep-ph].

[26] D. Gonçalves, J. H. Kim and K. Kong, *Probing the top-Higgs Yukawa CP structure in dileptonic $t\bar{t}h$ with M_2-assisted reconstruction*, JHEP **06** (2018) 079, arXiv: 1804.05874 [hep-ph].

[27] D. Azevedo, A. Onofre, F. Filthaut and R. Gonçalo, *CP tests of Higgs couplings in $t\bar{t}h$ semileptonic events at the LHC*, Phys. Rev. D **98** (2018) 033004, arXiv: 1711.05292 [hep-ph].

[28] A. Ferroglia, M. C. N. Fiolhais, E. Gouveia and A. Onofre, *Role of the $t\bar{t}h$ rest frame in direct top-quark yukawa coupling measurements*, Phys. Rev. D **100** (2019) 075034, arXiv: 1909.00490 [hep-ph].

[29] ATLAS Collaboration, *Measurement of Higgs boson decay into b-quarks in associated production with a top-quark pair in pp collisions at $\sqrt{s}$ = 13 TeV with the ATLAS detector*, JHEP **06** (2021) 097, arXiv: 2111.06712 [hep-ex].

[30] D. de Florian et al., *Handbook of LHC Higgs Cross Sections: 4. Deciphering the Nature of the Higgs Sector*, (2016), arXiv: 1610.07922 [hep-ph].

[31] ATLAS Collaboration, *The ATLAS Experiment at the CERN Large Hadron Collider*, JINST **3** (2008) S08003.

[32] ATLAS Collaboration, *ATLAS Insertable B-Layer: Technical Design Report*, ATLAS-TDR-19; CERN-LHCC-2010-013, 2010, URL: https://cds.cern.ch/record/1291633, Addendum: ATLAS-TDR-19-ADD-1; CERN-LHCC-2012-009, 2012, URL: https://cds.cern.ch/record/1451888.

[33] B. Abbott et al., *Production and integration of the ATLAS Insertable B-Layer*, JINST **13** (2018) T05008, arXiv: 1803.00844 [physics.ins-det].

[34] ATLAS Collaboration, *Performance of the ATLAS trigger system in 2015*, Eur. Phys. J. C **77** (2017) 317, arXiv: 1611.09661 [hep-ex].

[35] ATLAS Collaboration, *The ATLAS Collaboration Software and Firmware*, ATL-SOFT-PUB-2021-001, 2021, URL: https://cds.cern.ch/record/2767187.

[36] ATLAS Collaboration, *Performance of the ATLAS muon triggers in Run 2*, JINST **15** (2020) P09015, arXiv: 2004.13447 [hep-ex].

[37] ATLAS Collaboration, *Performance of electron and photon triggers in ATLAS during LHC Run 2*, Eur. Phys. J. C **80** (2020) 47, arXiv: 1909.00761 [hep-ex].

[38] ATLAS Collaboration, *Electron and photon performance measurements with the ATLAS detector using the 2015–2017 LHC proton–proton collision data*, JINST **14** (2019) P12006, arXiv: 1908.00005 [hep-ex].

[39] ATLAS Collaboration, *Muon reconstruction and identification efficiency in ATLAS using the full Run 2 pp collision data set at $\sqrt{s}$ = 13 TeV*, Eur. Phys. J. C **81** (2021) 578, arXiv: 2012.00578 [hep-ex].

[40] ATLAS Collaboration, *Topological cell clustering in the ATLAS calorimeters and its performance in LHC Run 1*, Eur. Phys. J. C **77** (2017) 490, arXiv: 1603.02934 [hep-ex].

[41] ATLAS Collaboration, *Jet energy scale and resolution measured in proton–proton collisions at $\sqrt{s}$ = 13 TeV with the ATLAS detector*, Eur. Phys. J. C **81** (2020) 689, arXiv: 2007.02645 [hep-ex].

[42] M. Cacciari, G. P. Salam and G. Soyez, *The anti-k_t jet clustering algorithm*, JHEP **04** (2008) 063, arXiv: 0802.1189 [hep-ph].

[43] M. Cacciari, G. P. Salam and G. Soyez, *FastJet user manual*, Eur. Phys. J. C **72** (2012) 1896, arXiv: 1111.6097 [hep-ph].

[44] ATLAS Collaboration, *ATLAS b-jet identification performance and efficiency measurement with $t\bar{t}$ events in pp collisions at $\sqrt{s}$ = 13 TeV*, Eur. Phys. J. C **79** (2019) 970, arXiv: 1907.05120 [hep-ex].

[45] ATLAS Collaboration, *Measurement of b-tagging efficiency of c-jets in $t\bar{t}$ events using a likelihood approach with the ATLAS detector*, ATLAS-CONF-2018-001, 2018, URL: https://cds.cern.ch/record/2306649.

[46] ATLAS Collaboration, *Calibration of light-flavour b-jet mistagging rates using ATLAS proton–proton collision data at $\sqrt{s}$ = 13 TeV*, ATLAS-CONF-2018-006, 2018, URL: https://cds.cern.ch/record/2314418.

[47] ATLAS Collaboration, *Performance of missing transverse momentum reconstruction with the ATLAS detector using proton–proton collisions at $\sqrt{s}$ = 13 TeV*, Eur. Phys. J. C **78** (2018) 903, arXiv: 1802.08168 [hep-ex].

[48] B. Nachman, P. Nef, A. Schwartzman, M. Swiatlowski and C. Wanotayaroj, *Jets from jets: re-clustering as a tool for large radius jet reconstruction and grooming at the LHC*, JHEP **02** (2015) 075, arXiv: 1407.2922 [hep-ph].

[49] ATLAS Collaboration, *The ATLAS Simulation Infrastructure*, Eur. Phys. J. C **70** (2010) 823, arXiv: 1005.4568 [physics.ins-det].

[50] GEANT4 Collaboration, S. Agostinelli et al., *GEANT4 – a simulation toolkit*, Nucl. Instrum. Meth. A **506** (2003) 250.

[51] T. Sjöstrand et al., *An introduction to PYTHIA 8.2*, Comput. Phys. Commun. **191** (2015) 159, arXiv: 1410.3012 [hep-ph].

[52] ATLAS Collaboration, *The Pythia 8 A3 tune description of ATLAS minimum bias and inelastic measurements incorporating the Donnachie–Landshoff diffractive model*, ATL-PHYS-PUB-2016-017, 2016, URL: https://cds.cern.ch/record/2206965.

[53] T. Ježo, J. M. Lindert, N. Moretti and S. Pozzorini, *New NLOPS predictions for $t\bar{t}$ + b-jet production at the LHC*, Eur. Phys. J. C **78** (2018) 502, arXiv: 1802.00426 [hep-ph].

[54] F. Cascioli, P. Maierhöfer and S. Pozzorini, *Scattering Amplitudes with Open Loops*, Phys. Rev. Lett. **108** (2012) 111601, arXiv: 1111.5206 [hep-ph].

[55] A. Denner, S. Dittmaier and L. Hofer, *COLLIER: A fortran-based complex one-loop library in extended regularizations*, Comput. Phys. Commun. **212** (2017) 220, arXiv: 1604.06792 [hep-ph].

[56] T. Ježo, *Powheg-Box-Res ttbb source code*, 2019, URL: https://gitlab.cern.ch/tjezo/powheg-box-res_ttbb/.

[57] R. D. Ball et al., *Parton distributions for the LHC run II*, JHEP **04** (2015) 040, arXiv: 1410.8849 [hep-ph].

[58] ATLAS Collaboration, *ATLAS Pythia 8 tunes to 7 TeV data*, ATL-PHYS-PUB-2014-021, 2014, URL: https://cds.cern.ch/record/1966419.

[59] ATLAS Collaboration, *Measurements of inclusive and differential fiducial cross-sections of $t\bar{t}$ production with additional heavy-flavour jets in proton–proton collisions at $\sqrt{s} = 13$ TeV with the ATLAS detector*, JHEP **04** (2019) 046, arXiv: 1811.12113 [hep-ex].

[60] CMS Collaboration, *Measurement of the $t\bar{t}b\bar{b}$ production cross section in the all-jet final state in pp collisions at $\sqrt{s} = 13$ TeV*, Phys. Lett. B **803** (2020) 135285, arXiv: 1909.05306 [hep-ex].

[61] P. Nason, *A new method for combining NLO QCD with shower Monte Carlo algorithms*, JHEP **11** (2004) 040, arXiv: hep-ph/0409146.

[62] S. Frixione, P. Nason and C. Oleari, *Matching NLO QCD computations with parton shower simulations: the POWHEG method*, JHEP **11** (2007) 070, arXiv: 0709.2092 [hep-ph].

[63] S. Alioli, P. Nason, C. Oleari and E. Re, *A general framework for implementing NLO calculations in shower Monte Carlo programs: the POWHEG BOX*, JHEP **06** (2010) 043, arXiv: 1002.2581 [hep-ph].

[64] H. B. Hartanto, B. Jäger, L. Reina and D. Wackeroth, *Higgs boson production in association with top quarks in the POWHEG BOX*, Phys. Rev. D **91** (2015) 094003, arXiv: 1501.04498 [hep-ph].

[65] M. Beneke, P. Falgari, S. Klein and C. Schwinn, *Hadronic top-quark pair production with NNLL threshold resummation*, Nucl. Phys. B **855** (2012) 695, arXiv: 1109.1536 [hep-ph].

[66] M. Cacciari, M. Czakon, M. Mangano, A. Mitov and P. Nason, *Top-pair production at hadron colliders with next-to-next-to-leading logarithmic soft-gluon resummation*, Phys. Lett. B **710** (2012) 612, arXiv: 1111.5869 [hep-ph].

[67] P. Bärnreuther, M. Czakon and A. Mitov, *Percent-Level-Precision Physics at the Tevatron: Next-to-Next-to-Leading Order QCD Corrections to $q\bar{q} \to t\bar{t} + X$*, Phys. Rev. Lett. **109** (2012) 132001, arXiv: 1204.5201 [hep-ph].

[68] M. Czakon and A. Mitov, *NNLO corrections to top-pair production at hadron colliders: the all-fermionic scattering channels*, JHEP **12** (2012) 054, arXiv: 1207.0236 [hep-ph].

[69] M. Czakon and A. Mitov, *NNLO corrections to top pair production at hadron colliders: the quark-gluon reaction*, JHEP **01** (2013) 080, arXiv: 1210.6832 [hep-ph].

[70] M. Czakon, P. Fiedler and A. Mitov, *Total Top-Quark Pair-Production Cross Section at Hadron Colliders Through $O(\alpha_S^4)$*, Phys. Rev. Lett. **110** (2013) 252004, arXiv: 1303.6254 [hep-ph].

[71] M. Czakon and A. Mitov, *Top++: A program for the calculation of the top-pair cross-section at hadron colliders*, Comput. Phys. Commun. **185** (2014) 2930, arXiv: 1112.5675 [hep-ph].

[72] P. Artoisenet et al., *A framework for Higgs characterisation*, JHEP **11** (2013) 043, arXiv: 1306.6464 [hep-ph].

[73] A. Alloul, N. D. Christensen, C. Degrande, C. Duhr and B. Fuks, *FeynRules 2.0 - A complete toolbox for tree-level phenomenology*, Comput. Phys. Commun. **185** (2014) 2250, arXiv: 1310.1921 [hep-ph].

[74] C. Degrande et al., *UFO - The Universal FeynRules Output*, Comput. Phys. Commun. **183** (2012) 1201, arXiv: 1108.2040 [hep-ph].

[75] J. Alwall et al., *The automated computation of tree-level and next-to-leading order differential cross sections, and their matching to parton shower simulations*, JHEP **07** (2014) 079, arXiv: 1405.0301 [hep-ph].

[76] R. Raitio and W. W. Wada, *Higgs-boson production at large transverse momentum in quantum chromodynamics*, Phys. Rev. D **19** (3 1979) 941.

[77] W. Beenakker et al., *NLO QCD corrections to $t\bar{t}H$ production in hadron collisions*, Nucl. Phys. B **653** (2003) 151, arXiv: hep-ph/0211352 [hep-ph].

[78] S. Dawson, C. Jackson, L. H. Orr, L. Reina and D. Wackeroth, *Associated Higgs boson production with top quarks at the CERN Large Hadron Collider: NLO QCD corrections*, Phys. Rev. D **68** (3 2003) 034022, arXiv: hep-ph/0305087v2 [hep-ph].

[79] Y. Zhang, W.-G. Ma, R.-Y. Zhang, C. Chen and L. Guo, *QCD NLO and EW NLO corrections to $t\bar{t}H$ production with top quark decays at hadron collider*, Phys. Lett. B **738** (2014) 1, arXiv: 1407.1110 [hep-ph].

[80] S. Frixione, V. Hirschi, D. Pagani, H.-S. Shao and M. Zaro, *Electroweak and QCD corrections to top-pair hadroproduction in association with heavy bosons*, JHEP **06** (2015) 184, arXiv: 1504.03446 [hep-ph].

[81] S. Frixione, E. Laenen, P. Motylinski and B. R. Webber, *Angular correlations of lepton pairs from vector boson and top quark decays in Monte Carlo simulations*, JHEP **04** (2007) 081, arXiv: hep-ph/0702198.

[82] ATLAS Collaboration, *Performance of jet substructure techniques for large-R jets in proton–proton collisions at $\sqrt{s} = 7$ TeV using the ATLAS detector*, JHEP **09** (2013) 076, arXiv: 1306.4945 [hep-ex].

[83] DØ Collaboration, *Measurement of the Top Quark Mass Using Dilepton Events*, Physical Review Letters **80** (1998) 2063, arXiv: 9706014 [hep-ex].

[84] ATLAS Collaboration, *Measurements of top-quark pair differential cross-sections in the $e\mu$ channel in pp collisions at $\sqrt{s} = 13$ TeV using the ATLAS detector*, Eur. Phys. J. C **77** (2017) 292, arXiv: 1612.05220 [hep-ex].

[85] ATLAS Collaboration, *Study of top-quark pair modelling and uncertainties using ATLAS measurements at $\sqrt{s} = 13$ TeV*, ATL-PHYS-PUB-2020-023, 2020, URL: https://cds.cern.ch/record/2730443.

[86] J. Bellm et al., *Herwig 7.0/Herwig++ 3.0 release note*, Eur. Phys. J. C **76** (2016) 196, arXiv: 1512.01178 [hep-ph].

[87] G. Cowan, K. Cranmer, E. Gross and O. Vitells, *Asymptotic formulae for likelihood-based tests of new physics*, Eur. Phys. J. C **71** (2011) 1554, arXiv: 1007.1727 [physics.data-an], Erratum: Eur. Phys. J. C **73** (2013) 2501.

[88] R. Cousins, *Generalization of Chisquare Goodness-of-Fit Test for Binned Data Using Saturated Models, with Application to Histograms*, 2013,
URL: http://www.physics.ucla.edu/~cousins/stats/cousins_saturated.pdf.